Superconductor
Science and
Technology

PAPER • **OPEN ACCESS**

Quantifying extended RE124 stacking faults in RE123 thin films using x-ray diffraction

To cite this article: Kai Walter *et al* 2026 *Supercond. Sci. Technol.* **39** 085027

Superconductor Science and Technology

OPEN ACCESS

RECEIVED
31 March 2026

REVISED
20 July 2026

ACCEPTED FOR PUBLICATION
11 August 2026

PUBLISHED
24 August 2026

PAPER

Quantifying extended RE124 stacking faults in RE123 thin films using x-ray diffraction

Kai Walter[1,*], **Mark Rikel**[2], **Martin Peterlechner**[3], **Manuela Erbe**[1], **Jens Hänisch**[1] and **Bernhard Holzapfel**[1]

[1] Institute for Technical Physics, Karlsruhe Institute of Technology, Karlsruhe 76131, Germany
[2] Faraday Factory Japan LLC, Hachioji, Tokyo, 192-0032, Japan
[3] Laboratory for Electron Microscopy, Karlsruhe Institute of Technology, Karlsruhe 76131, Germany
[*] Author to whom any correspondence should be addressed.

E-mail: kai.walter@kit.edu

Keywords: REBCO, RE124, SmBCO, CSD, XRD, stacking fault, stacking fault density

Abstract

Currently most optimizations of the superconducting properties of REBa$_2$Cu$_3$O$_{7-\delta}$ (REBCO, RE123) are done based on process parameters. Defect-density based methods offer a more direct way for such optimization due to the fact that the superconducting properties of a REBCO conductor emerge from its defect landscape. In this study, an x-ray diffraction (XRD) method will be presented that helps to determine the stacking fault density (SFD) of REBa$_2$Cu$_4$O$_8$ (RE124) stacking faults reasonably well. It is based on the fact that RE124 stacking faults introduce peak shifts and broadening to (00 l) reflections of RE123. Both quantities vary with the Miller index l, which enables the identification and quantification of these stacking faults. The method is tested using Sm123 thin film samples produced via chemical solution deposition (CSD). A Cu excess is used to facilitate the growth of extended Sm124 stacking faults through a high-temperature oxygenation. The resulting samples show exactly the behavior predicted by the presented theory. The SFDs determined via XRD are then cross-checked by transmission electron microscopy micrographs. It is found that the SFD from peak shift describes the majority of the samples to a sufficient degree of accuracy. Therefore, the presented method is applicable to quantify extended Re124 stacking faults in RE123 thin films.

1. Introduction

The superconducting performance of REBa$_2$Cu$_3$O$_{7-\delta}$ (REBCO, RE123) Coated Conductors (CCs) is largely determined by their defect landscape. A lot of work has already been done to identify beneficial and detrimental defects in REBCO bulk and film samples, some of the most important ones being oxygen vacancies [1–4], grain boundaries [5], nanoprecipitates like Y_2O_3 [6] and BaMO_3 (M=Zr, Hf) [7, 8], stacking faults [9, 10], and dislocations [11, 12]. Insights into these microstructures are obtained from transmission electron microscopy (TEM) studies, which, however, are most often just qualitative, because quantification of the defect landscape from TEM images needs expensive and time-consuming procedures. In addition, specimen preparation and electron beam induced heating during TEM observations may affect the defect landscape. Therefore, it is very beneficial to use non-destructive methods such as x-ray diffraction (XRD) for understanding and quantifying the defect state.

Extended stacking faults or intergrowth-like defects may cause essential changes in XRD patterns of layered structures that were studied since the late 1930s. Particularly applied in crystal chemistry, e.g. of layered clay minerals [13]. These methods were also applied to the HTS layered structures, first to $Bi_2Sr_2Ca_{n-1}Cu_nO_{2n+4+y}$ (BSCCO) [14–19], and later also to $YBa_2Cu_3O_{7-\delta}$ (YBCO) [20–23] but with limited success.

The RE123 c-axis stacking sequence BaO–CuO_2–RE–CuO_2–BaO–CuO is closely related to the stacking sequence of REBa$_2$Cu$_4$O$_8$ (RE124). An additional CuO chain layer is inserted above the CuO chain

layer of RE123, forming a stacking fault with respect to RE123 with a displacement vector of $[0, b/2, c/6]$ [9, 24]. The position of the additional CuO chain layer changes the coordination of the chain oxygen and thereby restricts its mobility, which is why the RE124 phase can retain its oxygen up to high temperatures as compared to the RE123 phase [25–27]. The extra CuO layer also increases the separation of the superconducting CuO_2 layers of adjacent RE123 unit cells, which increases the correlated pinning when the magnetic field B is parallel to the ab-plane, resulting in an increased $J_c(\theta)$ anisotropy [28]. Thus, it is important to understand and quantify the formation of extended RE124 stacking faults.

For this purpose, an analysis method is presented based on the work of Hendricks and Teller [29] for x-ray scattering of stacked crystals, which was adapted by Suzuki and Suzuki by applying a peak shape analysis [30]. This theoretical work will then be applied to Sm123 thin film samples by deliberately producing Sm124 stacking faults and determining their stacking fault density (SFD).

2. Theoretical background

In order to investigate stacking faults using XRD, understanding the scattered intensity of layered crystals is necessary. Alterations of the stacking sequence i.e. stacking faults, change the structure factor of the resulting crystal structure and disrupt the periodicity of the regular lattice. Thereby, stacking faults change the observed intensity by phase shifts of the scattered radiation. As shown by Hendricks and Teller [29], a layered crystal with randomly distributed layer types, or stacking faults for that matter, behaves like a regular crystal with an averaged scattering vector and additional scattering layers with scattering vectors equal to the difference between the average and real scattering vectors, compare equation (16) in appendix. Suzuki and Suzuki [30] realized that the term describing the additional layers can be brought into the form of a Lorentzian peak shape. With that, they opened a path to further dissecting the influence of stacking faults into changes to the peak positions i.e. peak shifts Δ_{PS}, and changes to the peak widths, broadening. Thus, stacking faults introduce Miller index-dependent, so-called asymmetric, Δ_{PS} and Δ_{FWHM}, which means that some reflections are more affected than others. A comprehensive summary and explanations of the derivations of [29] and [30] are given in appendix.

The basis of the approach presented in this study was already applied with varying success to the superconducting layered structures BSSCO [14–19] and $YBa_2Cu_3O_{7-\delta}$ (YBCO) [20–23]. While all these studies show the effect of stacking faults on the superconducting properties, most of them lack a full disclosure on how the stacking faults were quantified. To remedy this situation and to make the application of the approach presented here as straightforward as possible, the full derivation of the relevant equations will be shown in the following section.

The formulations by Suzuki and Suzuki directly enables one to investigate RE124 stacking faults in RE123 thin films. For that, two types of layers must be considered: dominant RE123 layers and RE124 layers formed by intercalated CuO chains. The differences in structure factors of both layers are neglected for this analysis, as they mainly influence the amplitude of the investigated Lorentzian peak shape. The main contribution to the peak shift and broadening due to intercalated CuO chains originates from the difference in stacking distances of both layer types, $\Delta c = c_{RE123} - c_F$. Therein, c_{RE123} describes the c-axis of the RE123 matrix and c_F the c-axis of the second layer along the stacking direction. c_F could be called c_{RE124} but this analysis should also be valid for other types of stacking faults with other characteristic lengths. So, c_F will be used to keep generality. The respective probabilities of occurring RE123 and RE124 layers are $1-f$ and f.

Plugging these parameters into the equations found by Suzuki and Suzuki, compare equations (34) and (35) in appendix, the peak shift Δ_{PS} and broadening Δ_{FWHM} are described by:

$$\Delta_{PS} = \frac{f}{1-f}\frac{1}{c_{RE123}}\sin\left(\frac{2\pi l}{c_{RE123}}\Delta c\right) = \frac{f}{1-f}\frac{1}{c_{RE123}}\sin\left(2\pi l\left(1-\frac{c_F}{c_{RE123}}\right)\right) \tag{1}$$

$$\Delta_{FWHM} = 2\frac{f}{1-f}\frac{1}{c_{RE123}}\left(1-\cos\left(\frac{2\pi l}{c_{RE123}}\Delta c\right)\right) = 2\frac{f}{1-f}\frac{1}{c_{RE123}}\left(1-\cos\left(2\pi l\left(1-\frac{c_F}{c_{RE123}}\right)\right)\right). \tag{2}$$

The peak shift of (00l) peaks relative to the dominant phase can also be described as:

$$\Delta_{PS} = q(l) - q_{RE123} = \frac{2\pi}{d(l)} - \frac{2\pi}{d_{RE123}} = 2\pi l\left(\frac{1}{c(l)} - \frac{1}{c_{RE123}}\right). \tag{3}$$

Thus, equation (1) can be transformed from reciprocal space into real space:

$$2\pi l\left(\frac{1}{c(l)} - \frac{1}{c_{RE123}}\right) = \frac{f}{1-f}\frac{1}{c_{RE123}}\sin\left(2\pi l\left(1-\frac{c_F}{c_{RE123}}\right)\right) \tag{4}$$

$$c(l) = c_{\mathrm{RE123}}\left(1 + \frac{f}{1-f}\frac{\sin\left(2\pi l\left(1-\frac{c_{\mathrm{F}}}{c_{\mathrm{RE123}}}\right)\right)}{2\pi l}\right)^{-1}. \tag{5}$$

Equation (5) shows that the apparent c lattice parameter for each (00 l) peak oscillates around c_{RE123}. The amplitude and the wavelength of this oscillation depend on the frequency of the stacking faults f and on the ratio $c_{\mathrm{F}}/c_{\mathrm{RE123}}$. Hence, by fitting the parameters c_{RE123}, c_{F} and f, a deeper understanding of stacking faults can be gained. The SFD i.e. the number of faults per unit length along the c-direction, is found by:

$$\mathrm{SFD} = \frac{f}{f * c_{\mathrm{F}} + (1-f) * c_{\mathrm{RE123}}}. \tag{6}$$

The broadening due to stacking faults, Δ_{FWHM}, equation (2), influences the integral widths β of each (00l) reflection. These are usually analyzed using the Williamson–Hall method [31]. As a first approach, a simple linear combination of broadening due to crystallite size D, microstrain e, and stacking faults was done by transforming equation (2) into (θ)-space using $q = 2\pi l/c_{\mathrm{RE123}} = 4\pi\sin(\theta)/\lambda$:

$$\beta = \frac{1}{D} + \frac{4\pi}{\lambda}e\sin(\theta) + 2\frac{f}{1-f}\frac{1}{c_{\mathrm{RE123}}}\left(1-\cos\left(\frac{4\pi}{\lambda}\left(c_{RE123}-c_F\right)\sin(\theta)\right)\right). \tag{7}$$

The presented approach predicts that the peak shift and broadening increase with increasing SFD. This holds for small SFD because the averaged structure factor is dominated by the structure factor of the RE123 phase, compare equations (25) and (29) appendix. Experiments [20, 21, 32–35] show that so-called asymmetric shoulder peaks emerge at higher SFDs, figure 1(a)). Thus, a given reflection, e.g. (005), needs to be fitted using two peaks, $2\theta^{005}_{\mathrm{RE123}}$ and $2\theta^{005}_{\mathrm{RE124}}$, figure 1(b)), to describe the scattered intensity completely. This renders the peak shape analysis by Suzuki and Suzuki inapplicable because the peak overlap of $2\theta^{005}_{\mathrm{RE123}}$ and $2\theta^{006}_{\mathrm{RE124}}$ cannot be accounted for.

To solve this predicament and to extend the applicability of equation (5), we propose an averaging weighted by integral intensities, $I^{\mathrm{Int}}_{\mathrm{RE123}}$ and $I^{\mathrm{Int}}_{\mathrm{RE124}}$ to calculate a single $c(l)$ per reflection, equation (8), making it possible to calculate a peak shift even with shoulder peaks.

Averaging the broadening is not similarly straight forward. We tried multiple averaging methods for the integral widths of both peaks but found no sensible approach. The integral width of a peak depends on its maximum intensity. In order to average the integral widths of RE123 and RE124, a maximum intensity must be assumed. This introduces a degree of freedom that makes the choice of the maximal intensity arbitrary. To test equation (7), we decided to calculate a combined integral width by dividing the combined area of the RE123 and RE124 peaks by the maximum intensity of the RE123 peak. Using different maximum intensities did not lead to significant trend changes because only a subset of peaks with fitted shoulder peaks was affected.

$$2\theta^{00l}_{\mathrm{ave}} = \frac{I^{\mathrm{Int}}_{\mathrm{RE123}}2\theta^{00l}_{\mathrm{RE123}} + I^{\mathrm{Int}}_{\mathrm{RE124}}2\theta^{00l}_{\mathrm{RE124}}}{I^{\mathrm{Int}}_{\mathrm{RE123}} + I^{\mathrm{Int}}_{\mathrm{RE124}}}. \tag{8}$$

These approaches were tested by simulating XRD patterns using the FAULTS software [36], figure 1(c)), and fitted them by symmetric pseudo-Voigt peak shape functions in SmartlabStudio II provided by Rigaku. FAULTS uses the mathematical framework of Hendricks and Teller [29] and the computational approach of the DIFFAX program [37]. As figure 1(d)) shows, the averaged-peak approach determines the simulated SFD with a high degree of accuracy, and equation (5) can therefore be applied beyond the single-peak regime, blue dashed line.

Regarding the broadening, the simulations revealed that equation (7) can describe the asymmetric broadening of the RE123 matrix peaks. However, as will be shown and discussed later, the stacking fault frequency determined by broadening f_{FHWM} is consistently magnitudes smaller than that by peak shift.

The limit of the presented theory is reached when the SFD is around 0.20 nm^{-1}, which equates to one SF every four unit cells. At this point, the RE124 shoulder peaks are so far away from their respective RE123 peaks that barely any overlap occurs and RE123 can no longer be considered the dominant phase, which strictly means that equations (5) and (7) can no longer be applied. In such a scenario, an XRD pattern is more accurately described by two independent phases.

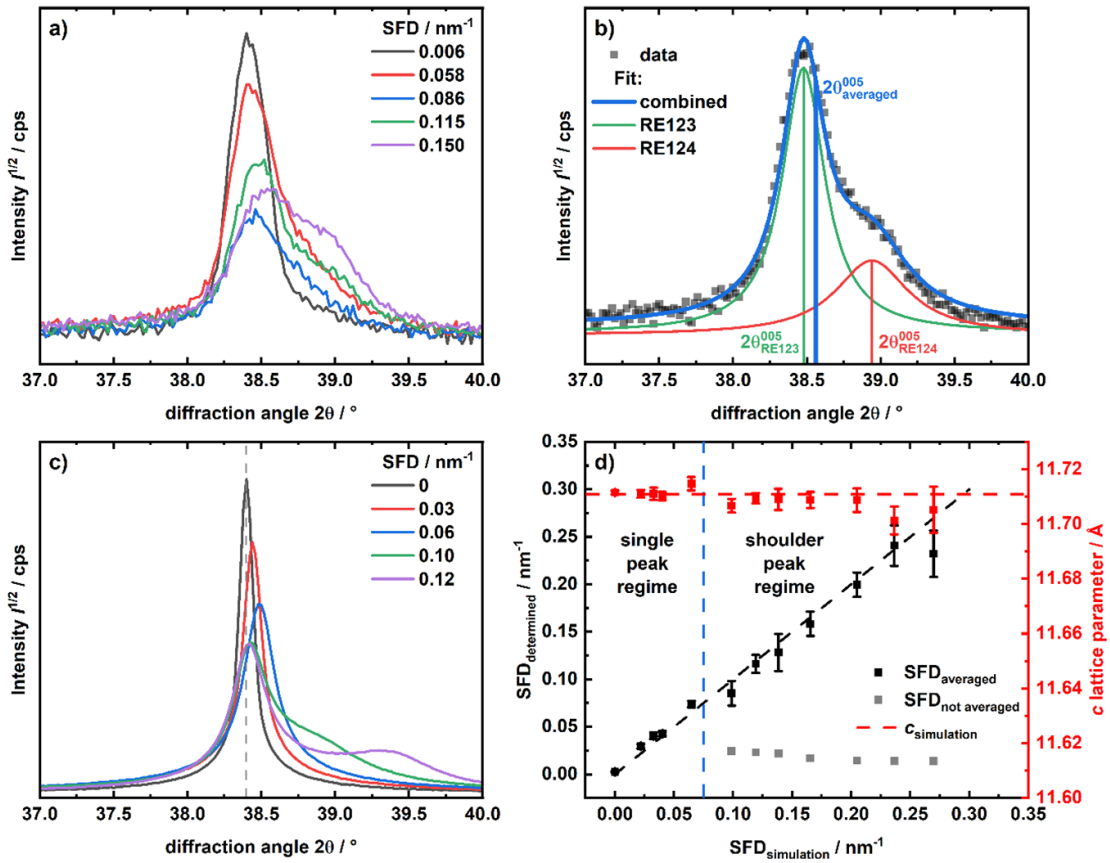

Figure 1. Influence of RE124 stacking faults on XRD patterns and the presented analysis. (a) Measured (005) reflections of Sm123 thin films with increasing SFD. (b) Exemplary fit of the (005) reflection. The fitted and averaged peak positions are given with vertical lines. (c) Simulated (005) reflections of *c*-axis oriented Sm123 with increasing SFD. At higher SFD additional shoulder peaks emerge while at small SFD only a peak shift occurs. (d) Comparison of simulated SFD vs determined SFD using equation (5). The red and black dashed lines represent c_{Sm123} used for the simulation and the identity of SFD, while the grey dashed line separates the single peak and averaged peak regime.

3. Experimental methods

In order to investigate the validity of the proposed analysis, $SmBa_2Cu_3O_{7-\delta}$ (Sm123) thin film samples were prepared by Chemical Solution Deposition (CSD) using metal-organic trifluoroacetate solutions based on methanol as a solvent. The solution chemistry is described in greater detail in [38]. Preliminary experiments revealed that solutions with a ratio of 1:2:3 for Sm, Ba, and Cu showed little potential to form Sm124 stacking faults. Therefore, two solutions with ratios 1:2:3.5 and 1:2:3.75 were prepared. This was done by mixing the standard 1:2:3 solution with a total ion concentration of 1.5 mol l^{-1} with a 1:2:4 stock solution with a total ion concentration of 1.6 mol l^{-1}.

The 1:2:3.5 and 1:2:3.75 solutions were spin-coated onto cleaned 10 × 10 mm^2 [100]-oriented $LaAlO_3$ (LAO) single crystal substrates with a rotational speed of 6000 rpm and a duration of 30 s to achieve film thicknesses of approx. 200(15) nm. After coating, these samples were pyrolyzed and crystallized, for more details refer to [39]. The crystallization of all samples was done at 820 °C and an oxygen partial pressure $p(O_2)$ of 50 ppm. Previous studies [20, 21, 32, 34, 40] suggested that the temperature T_{oxy}, time t_{oxy}, and oxygen partial pressure $p(O_2)_{oxy}$ during the oxygenation step play an important role in the formation of stacking faults. T_{oxy} ranged from 700 to 850 °C. t_{oxy} was kept constant at 12 h and was extended to 18 h or 24 h for some samples, table 1. $p(O_2)_{oxy}$ was kept constant at 1 bar to increase the probability of Sm124 stacking fault formation. The samples were furnace-cooled at a mean cooling rate of 2 K min^{-1} after t_{oxy} elapsed. Each run was performed with two samples simultaneously to evaluate the reproducibility of the presented procedure. This way, thin films with SFDs ranging from 0 to 0.20 nm^{-1} were produced. A detailed analysis of the formation conditions of stacking faults in REBCO thin films will be presented elsewhere.

The XRD investigations of all thin film samples were carried out using parallelized, monochromatic Cu-$K_{\alpha 1}$ radiation at 40 kV and 30 mA at a Rigaku Smartlab 3 kW device. The *c* lattice parameter was

Table 1. Solution type and oxygenation conditions for presented samples. The sample names give the figures in which the sample data are plotted.

Sample	Solution composition	T_{oxy} (°C)	t_{oxy} (h)	Sample	Solution composition	T_{oxy} (°C)	t_{oxy} (h)
Figures 3–1	1:2:3.50	—	—	Figures 6–1	1:2:3.50	800	24
Figures 3–2	1:2:3.50	800	24	Figures 6–2	1:2:3.75	750	12
Figures 4–1	1:2:3.50	800	12	Figures 7–1	1:2:3.50	850	12
Figures 4–2	1:2:3.75	800	24	Figures 7–2	1:2:3.50	825	12
Figures 4–3	1:2:3.75	800	12	Figures 7–3	1:2:3.50	750	12
Figures 4–4	1:2:3.50	800	24	Figures 7–4	1:2:3.75	800	24
Figures 4–5	1:2:3.75	750	12	Figures 7–5	1:2:3.50	700	12
Figure 5	1:2:3.50	—	—	Figures 7–6	1:2:3.75	800	24

determined using $\theta/2\theta$ scans ranging from $2 = 5°$ to 120° with a measurement speed of 1.75° min^{-1}. The resulting data sets were fitted using symmetric pseudo-Voigt peak shape functions implemented in Smartlab Studio II provided by Rigaku. The integral width β of each fitted peak was corrected for instrumental broadening assuming the Lorentzian shape ($\beta = \beta_{meas} - \beta_{instr}$).

Microbridges of 1 mm length and 20–30 μm width were prepared by photolithography and wet-chemical etching with the contact patches coated with gold for transport measurements in a four-point geometry to determine the anisotropy of the critical current density $J_c(\theta)$, where θ is the angle between the applied magnetic field B and the crystallographic c-axis i.e. the substrate normal. Each sample was measured at 77, 65, and 50 K at magnetic fields in the range of 1–14 T. Thin microbridges were chosen to minimize heating effects and to measure small critical currents I_c to avoid the current limit of 1 A of the measurement setup. This, however, lead to the case that complete $J_c(\theta)$ anisotropy curves were not measurable for all samples at magnetic fields above 3 T and higher temperatures as I_c was too small in these cases. Therefore, only the 1 and 3 T curves are shown here to evaluate the influence of stacking faults on $J_c(\theta)$. Thereby, J_c was determined using the cross-sectional area and the critical current, which was determined at $I(U = 10\mu V)$.

TEM was carried out using a FEI Titan 60–300 and a FEI Osiris working at 300 and 200 kV, respectively. High-resolution TEM (HRTEM) and Scanning TEM (STEM) was made using the Titan including an image CS-corrector and a TVIPS XF416 CMOS camera. Also STEM and energy dispersive x-ray (EDX) analysis was done using the Osiris including a ChemiSTEM (0.7 sr, 4 detectors) and a Fischione M3000 HAADF detector. The EDX analysis was made using the Bruker Esprit (2.3.1) software, and images were processed using Gatan GMS (3.62) and python-based script using HyperSpy [41]. A non-linear image filter, as introduced by Du [42], was applied to STEM images to reduce noise. Thin lamellae for TEM were prepared with an FEI Helios G4 Focused Ion Beam (FIB), using C and Pt protection layers, comparably low Ga currents and tilting for the final polishing steps. This minimizes curtaining effects and surface-damage layers.

4. Results

In order to study the applicability of the presented theory, thin film samples with extended Sm124 stacking faults needed to be produced. Figure 2(a)) shows a representative XRD pattern of a sample with a large number of stacking faults. The asymmetric behavior of the Sm124 reflections can be clearly seen. The (005) reflection has a Sm124 shoulder reflection on the right side, while the (007) reflection exhibits a Sm124 shoulder reflection on the left side. The (006) reflection does not show any shoulder because the Sm123 (006) and Sm124 (007) reflections coincide. The same holds for the (00$\underline{12}$) reflection of Sm123 (not shown in figure 2(a))), which is the reason why the peak positions and widths of the SmBCO (006) and (00$\underline{12}$) reflections are least affected by Sm124 stacking faults [32].

Weak reflections of secondary phases are visible between 29° and 37° and are identified as Sm_2O_3, CuO and Sm_2CuO_4 by comparison to the TEM data. Sm_2O_3 and CuO are most likely the decomposition products of Sm_2CuO_4 triggered by the high temperature oxygenation [43, 44]. It follows that the excess Cu of the CSD solutions leads to the formation of Sm124 stacking faults and Sm_2CuO_4.

The introduction of Sm124 stacking faults also influences the transition behavior, figure 2(b)). Sm123 thin films usually exhibit sharp transitions at a T_c of. The addition of Sm124 stacking faults lowers T_c and broadens the transition. This is to be expected, because the RE124 phase generally has a lower T_c than RE123. The transition broadens due to the fact that the phase homogeneity of the SmBCO thin films decreases. This effect is further enhanced by the solution chemistry. The samples

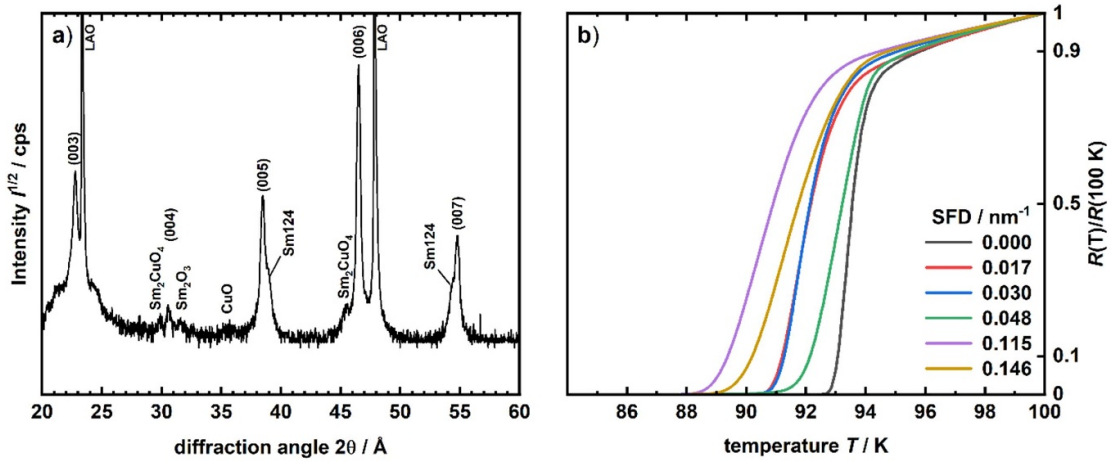

Figure 2. Representative SmBCO XRD pattern and $R(T)$ -curves. (a) The (00 l) reflections of SmBCO are indicated by their (hkl). The reflections of identified secondary phases are solely indexed by name. The Sm124 shoulder peaks emerge due to a high amount of Sm124 stacking faults. (b) $R(T)$ -curves of SmBCO thin films with a varying amount of Sm124 stacking faults. The addition of stacking faults broadens the transition and shifts it to lower temperatures.

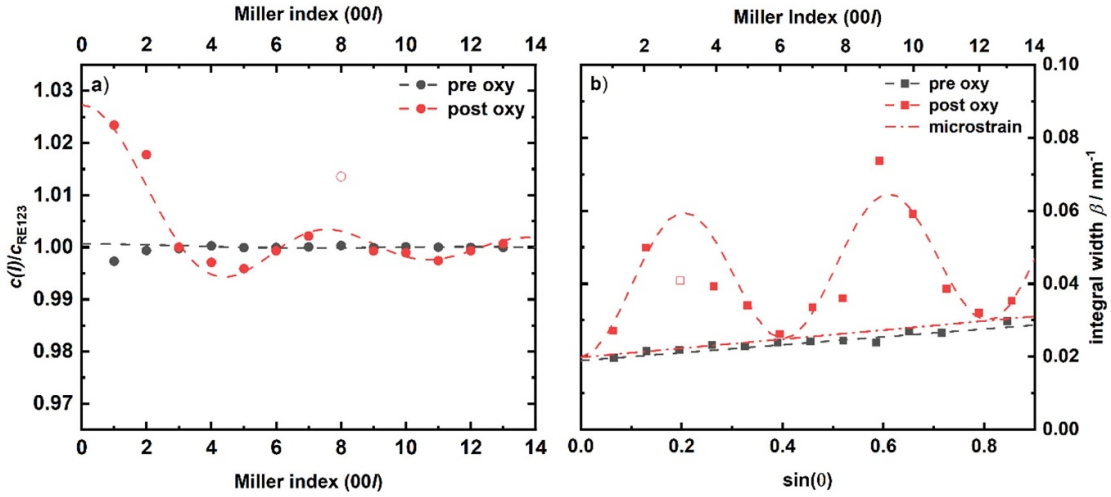

Figure 3. XRD analysis of the stacking fault formation due to high temperature oxygenation. (a) Peak shift analysis, equation (5) (b) Broadening analysis via a Williamson–Hall-Plot, equation (7). The grey and red data points represent the state before and after oxygenation, respectively, and the outliers are plotted as empty symbols. The oxygenation at high temperatures introduces stacking faults, which lead to an asymmetric peak shift and broadening. The wavelength of the oscillation can be explained accurately by Sm124 stacking faults. The fit parameters of both plots are given below in table 2.

of the 1:2:3.75 solution show a higher density of secondary phases, which is why their transitions are broader, green and yellow in figure 2(b)).

According to the literature, the oxygenation plays a crucial role for the stacking fault formation in REBCO films [32, 34, 45, 46]. Our experiments show the same behavior, figure 3. The grey and red data points represent the state before and after the oxygenation of a representative sample. Figure 3(a)) shows the peak shift of the (00 l) reflections. As a result of the oxygenation, the ratio $c(l)/c_{\mathrm{RE123}}$ clearly oscillates around unity, which is in accordance with the theory, equation (5).

However, the oscillating behavior alone does not suffice to identify the underlying stacking fault type. Different types of stacking faults such as RE124 or $RE_2Ba_2Cu_3O_8$ (RE223) [9, 47] produce different wavelengths through the ratio $c_{\mathrm{F}}/c_{\mathrm{RE123}}$. Sm124 stacking faults should produce a wavelength of six or a ratio of $\sim 7/6$ due to the displacement vector of an intercalated CuO layer. Another identifier of Sm124 stacking faults is the fact that the peak positions of (006) and (00$\underline{12}$), figure 3(a)), are not shifted [20, 32]. Both indicators are fulfilled for the samples presented in this work, which is strong evidence for the presence of Sm124 stacking faults due to the oxygenation at high temperatures.

The integral width, figure 3(b)), reveals significant, asymmetric peak broadening upon introducing stacking faults. In the pre-oxy state (grey dotted line), the broadening can solely be explained by the

Table 2. Fit parameters for the peak shift analysis, equation (5), and for the broadening analysis, equation (7). f stands for the stacking fault frequency fitted for each analysis. The sample name gives the figure in which the sample's data are plotted. The estimated standard deviations are given in brackets.

	Peak shift analysis				Broadening analysis		
Sample	c_{RE123} (Å)	c_F (Å)	f_{PS}	SFD (nm^{-1})	D (nm)	e (10^{-4})	f_{FWHM}
Figures 3–1	11.8380(7)	13.03(17)	0.0062(21)	0.0027	53(2)	1.32(15)	0.0003(2)
Figures 3–2	11.7138(64)	13.62(5)	0.1404(85)	0.1172	50(11)	1.53(85)	0.0108(15)
Figures 4–1	11.7128(14)	13.65(3)	0.0542(35)	0.0457	43(5)	0.36(58)	0.0032(8)
Figures 4–2	11.7066(38)	13.64(6)	0.0743(62)	0.0627	56(10)	2.12(57)	0.0045(9)
Figures 4–3	11.7162(24)	13.65(3)	0.1030(37)	0.0864	67(27)	4.59(135)	0.0103(20)
Figures 4–4	11.7138(64)	13.62(5)	0.1404(85)	0.1172	50(11)	1.53(85)	0.0108(15)
Figures 4–5	11.7133(92)	13.69(5)	0.1878(56)	0.1554	34(9)	2.13(161)	0.0224(29)
Figure 5	11.8437(4)	13.21(13)	—	—	48(1)	0.40(9)	—
Figures 6–1	11.7138(64)	13.62(5)	0.1404(85)	0.1172	50(11)	1.53(85)	0.0108(15)
Figures 6–2	11.7076(46)	13.67(8)	0.0606(27)	0.0512	52(2)	1.20(14)	0.0021(2)
Figures 7–1	11.7066(6)	13.61(7)	0.0109(31)	0.0093	44(1)	0.05(8)	0.0002(1)
Figures 7–2	11.7104(6)	13.64(3)	0.0203(12)	0.0173	50(3)	0.27(23)	0.0010(4)
Figures 7–3	11.7128(13)	13.64(5)	0.0363(23)	0.0308	51(5)	0.66(38)	0.0015(5)
Figures 7–4	11.7095(24)	13.67(5)	0.0574(42)	0.0486	46(5)	1.36(50)	0.0030(8)
Figures 7–5	11.7087(36)	13.64(3)	0.1389(50)	0.1159	56(9)	1.71(55)	0.0119(10)
Figures 7–6	11.7047(26)	13.66(16)	0.1767(133)	0.1466	40(17)	0.03(8)	0.0201(48)

crystallite size D (inverse of y-intercept) and microstrain e (linear slope) along the c-direction. Upon oxygenation, β starts to oscillate (red dashed line) while D and e stay relatively constant at 50 nm and $1.53^{*}10^{-4}$ (slope of red dash-dotted line). The microstrain and crystallite size of most samples are unaffected by the stacking fault formation. Not all samples show this trend. Some samples exhibit a significantly reduced microstrain after oxygenation. This could be explained by findings of Holesinger *et al* [45] and Zhu *et al* [48]. Both groups found that short-ranged stacking faults help to relieve strain around precipitates after oxygenation. In any case, the determined D and e values in figure 3(b)) must be interpreted cautiously, because the uncertainty of all fit parameters increases drastically through an increasing number of stacking faults.

Every sample subjected to high-temperature oxygenation exhibits a behavior similar to that presented in figure 3. Plotting the peak shift and broadening shows that both quantities increase with the stacking fault frequency f, figure 4. The plots are stacked to aid visibility. The oscillations of the asymmetric peak shift, figure 4(a)), and broadening, figure 4(b)), become more pronounced as f increases, while the ratio c_F/c_{RE123} assumes values of ∼7/6. The peak shift is most noticeable at the (005), (007), (00$\underline{11}$) and (00$\underline{13}$) reflections. The apparent c lattice parameters c_{005} and $c_{00\underline{11}}$ are always smaller than c_{007} and $c_{00\underline{13}}$, respectively.

The asymmetric broadening is most pronounced in the interval between the (005) and (00$\underline{12}$) reflections. Within this interval, the (009) reflection is broadened the most. Furthermore, an increased number of outliers or missing reflections occurs at high f values due to insufficient signal-to-noise ratios. Reflections with less intensity can be explained by the fact that large amounts of stacking faults heavily disrupt the coherently scattering volume, thereby lowering the intensity.

The sample with the highest stacking fault frequency (purple) has barely enough reflections to achieve satisfactory fits for both analyses, illustrating the limitations of the presented approach. In addition, this sample shows a volume fraction of Sm124 stacking faults that technically violates the assumption of equations (5) and (7). A stacking fault frequency of $f = 0.188$ means that stacking faults should occur every 6 nm or every 5th Sm123 unit cell. The volume fraction of Sm124 can, thus, no longer be regarded as small. So, while the averaging approach presented above helps to extend the applicability of equation (5) to higher SFD, it is not extended indefinitely und should be critically reviewed upon analysis. Nevertheless, figure 4 shows that the peak shift and broadening analysis can be applied to real thin-film samples with satisfactory results.

STEM micrographs of representative cross-sections, figures 5 and 6, were obtained to investigate the validity of our XRD findings. The FIB lamella preparation for TEM showed bending of the samples during thinning, which indicates that residual stresses either from the SFs, nanoparticles or other defect relaxation upon lamella preparation. This results in unequal contrasts over the field-of-view in the micrographs and made the imaging of SF frequently difficult. Multiple attempts were made to improve the image quality.

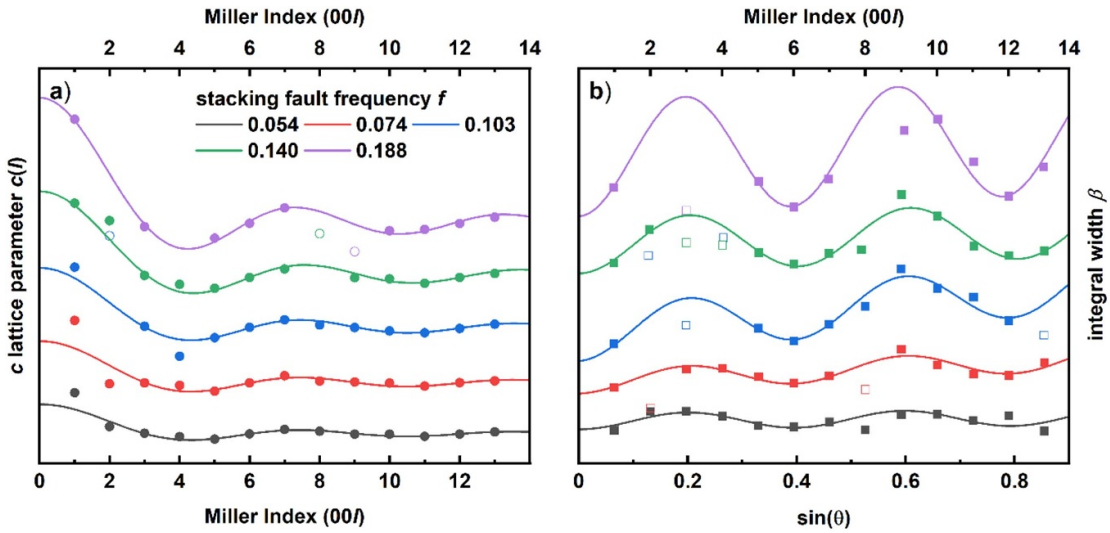

Figure 4. Peak shift and broadening analysis for representative samples. (a) The lattice parameters c calculated from each (00 l) reflection $c(L)$ vs. their respective Miller index l. (b) Integral widths β over sin (θ) as a Williamson–all plot. Each data set was fitted using equation (5) (a) or 7 (b). The plots were stacked to aid visibility, and outliers were plotted in empty symbols. The oscillations increase as the stacking fault frequencies f increase. The presented theory is able to fit and explain the observed behavior accurately. The fitted parameters of both plots are given in table 2.

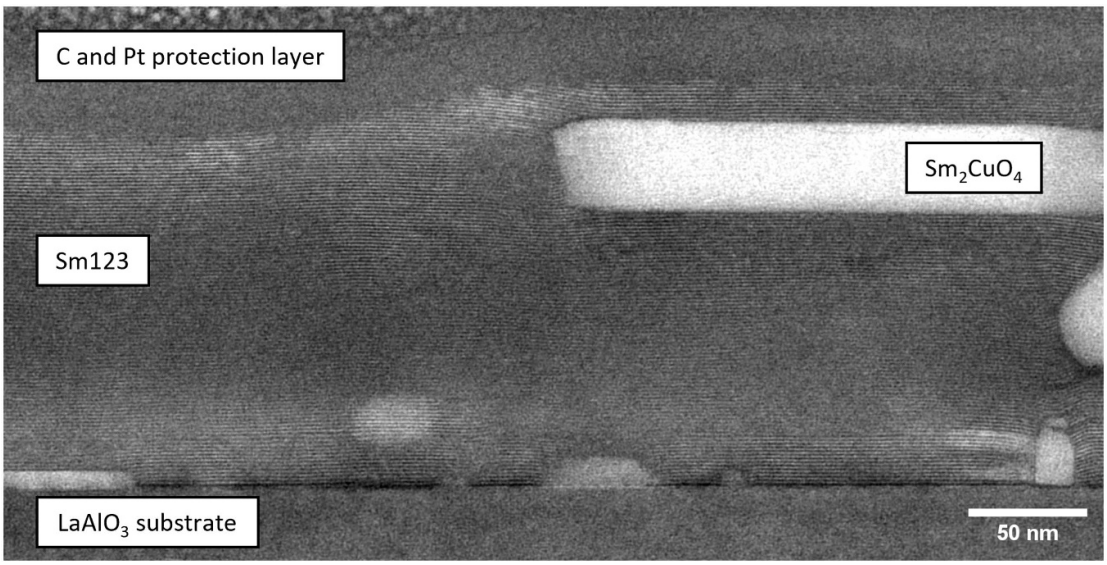

Figure 5. STEM HAADF micrograph of a representative sample before oxygenation. Facetted and circular nanoparticles are imbedded in the Sm123 matrix. Heavily bent lattice planes of Sm123 are visible around the edges of the facetted nanoparticles. Those are identified as Sm_2CuO_4, while the circular nanoparticles are either Sm_2O_3 or CuO.

In spite of that, insights are gained from the micrographs on the SFD and precipitates. The state before the oxygenation at high temperatures is characterized by c-axis-textured, oxygen-deficient Sm123 interlaced with circular as well as facetted nanoparticles, at which some of the lattice planes of Sm123 show strong bending, figure 5.

The XRD patterns hint at nanoparticles, but the low intensity of their reflections makes their identification by XRD alone uncertain. The TEM analysis solved this problem. EDX revealed that the circular nanoparticles are either Sm_2O_3 or CuO while the facetted nanoparticles are enriched in Sm. Relative to the Sm123 matrix, they contain less Cu and no Ba, but the region below such particles is slightly enriched with Ba, figure 6(c)). Knowing that Sm–Cu–O particles are present in the films, the reflections at 29.9 and 45.5° in figure 2(a)) are clearly assigned to Sm_2CuO_4 (004) and (006).

The textured nature of the Sm_2CuO_4 nanoparticles is in line with the similar crystal structures of Sm_2CuO_4 and Sm123 and an orientation relationship between matrix and precipitates. Both unit cells share CuO layers as well as similar symmetries and lattice parameters. The (00 l) texture of Sm123 is

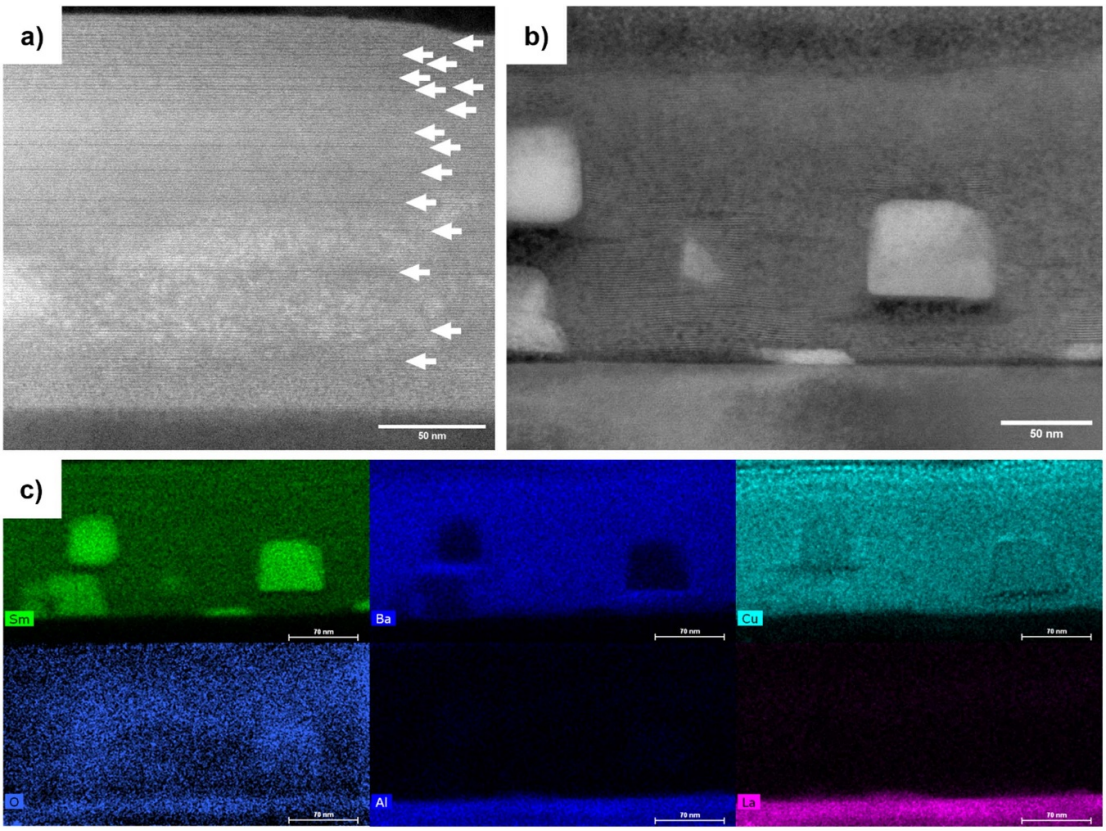

Figure 6. STEM micrographs and EDX data of the post-oxy microstructure. The microstructure after the oxygenation shows either (a) a lot of extended stacking faults (white arrows) or (b) Sm_2CuO_4 nanoparticles that distort the Sm123 matrix around them. No extended stacking faults are found in the vicinity of Sm_2CuO_4 nanoparticles. However, indications for short stacking faults are visible (yellow arrows) (c) EDX count maps of the area shown in (b) show Sm-rich precipitates.

therefore transferred to the semi-coherent Sm_2CuO_4 nanoparticles This process causes the lattice planes of Sm123 to bend significantly at the nanoparticle interface.

Selected area electron diffraction (SAED) patterns of the precipitates were made. The information content of these is limited due to different reasons. Firstly, the precipitates are not free-standing and thus, always influenced by the strongly bent lattice around them. Especially in thicker samples (>50 nm), double diffraction between the severely bent matrix and the precipitates blurs the reflections massively. Due to that, indexing the SAED patterns becomes practically difficult as finding a proper zones axis is hard to identify. Within limits, the observed reflections agree with the interpretations we made from the XRD and STEM-EDX data.

The high-temperature oxygenation produced two types of microstructures. Either no nanoparticles and large numbers of extended stacking faults, figure 6(a)), or Sm_2CuO_4 nanoparticles and insignificant numbers of stacking faults are observed, figure 6(b)). The XRD patterns reveal that samples showing lots of SFs in TEM also have Sm_2CuO_4 reflections and vice versa. Hence, the SF formation and occurrence of Sm_2CuO_4 maybe be locally related but not across an entire film. Based on the XRD analysis, a holistic microstructure representation is gained. Overall, this shows the strength of the combination of an integral XRD measurement with a local TEM analysis for SF characterization, identification and quantification, as well as the precipitate analysis.

The unknown effect of Sm_2CuO_4 nanoparticles on the stacking fault formation prompts new working hypotheses that require further investigation in future work. The semi-coherent interface of Sm_2CuO_4 could strain the surrounding Sm123 matrix in such a way that the intercalation of CuO layers becomes unstable. The second point that needs clarification is the chemical distribution of Cu. In-depth EDX and electron energy loss spectroscopy (EELS) studies are needed to locate the excess Cu. Investigating these points will help to understand how RE124 stacking faults form in RE123 thin films.

Regardless, the combined TEM and XRD results show that the microstructure of the presented Sm123 thin films is dominated by stacking faults and nanoparticles. While the nanoparticles contribute to the microstrain within the Sm123 phase, they do not produce asymmetric peak shifts and asymmetric broadening. Because stacking faults are the only remaining microstructural feature as detected by

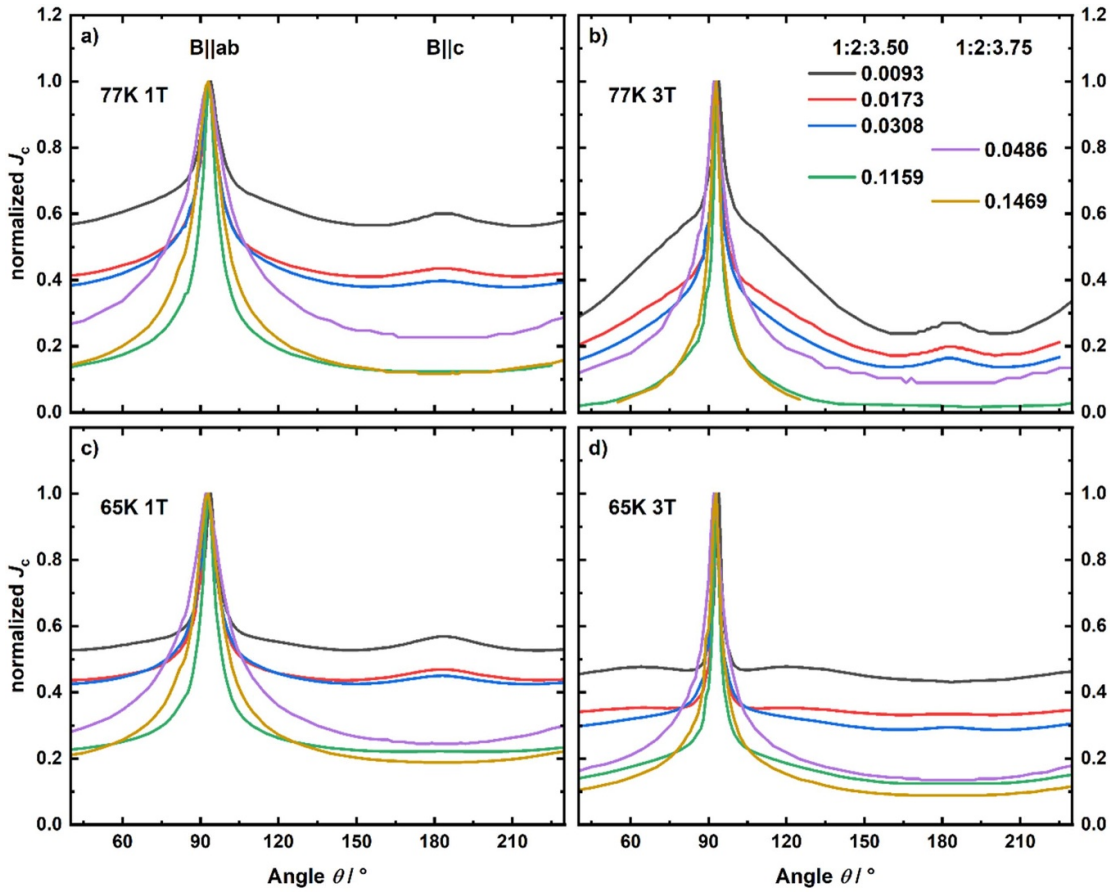

Figure 7. Normalized anisotropy plots for 77 K (a) 1 T, (b) 3 T and 65 K (c) 1 T and (d) 3 T. The legend gives the stacking fault density SFD in nm^{-1} and solution type for each sample. The plots are normalized to $J_c(\theta = 90°)$ (B||*ab*). Correlated pinning at B||*ab* become stronger, while the peak at B||*c* is suppressed with an increasing SFD. Samples produced with the 1:2:3.75 solution exhibit broader B||*ab* peaks due to additional pinning defects such as secondary phases.

TEM, we conclude that exactly these extended Sm124 stacking faults are responsible for the observed peak shifts and broadening presented in figures 3 and 4.

Having identified Sm124 stacking faults as the dominant microstructural feature and being able to determine their SFD opens many new investigation possibilities. On the one hand, it is possible to investigate the conditions needed to produce extended stacking faults within thin films. On the other hand, the influence of extended stacking faults on the superconducting behavior may be studied in greater detail.

A preliminary investigation of the influence of oxygenation temperature T_{oxy} and time t_{oxy} on the stacking fault formation has shown that the highest SFD in Sm123 can be reached for T_{oxy} of 750 °C –800 °C. Nevertheless, some samples show drastically different SFDs even when oxygenated under the same conditions. The TEM insights and the results of these preliminary investigations lead us to believe that the microstructure prior to the oxygenation plays a major role in how many SFs form. For example, a large number of Sm_2CuO_4 particles prior to the oxygenation leads to drastically reduced amounts of Cu that could be intercalated, and hence, a reduced amount of RE124 stacking faults is to be expected. Although the samples presented here suffice to show the applicability of the method to determine stacking fault densities, the results of our preliminary investigations are by no means expansive enough to allow for decisive conclusions. A more rigorous study is planned to systematically investigate the influence of the oxygenation conditions on the stacking fault formation.

The investigations of the superconducting state reveal a distinct influence of Sm124 stacking faults on the $J_c(\theta)$ anisotropy of SmBCO thin films. Figure 7 shows $J_c(\theta)$ for 77 and 65 K at 1 and 3 T each. The plots are normalized to $J_c(\theta = 90°)$. The anisotropy of $J_c(\theta)$ arises from the crystal structure of REBCO and its microstructure, i.e. from pinning-active defects. Such defects may contribute uniformly to $J_c(\theta)$ over the entire angular range of the magnetic field, $J_{c,n,random}$. They may also be correlated within the crystal structure and thus contribute to $J_c(\theta)$ only in specific crystallographic directions, i.e. if the magnetic field is aligned along certain directions, mainly $J_{c,n,B||ab}$ and $J_{c,n,B||c}$, figure 8(a)).

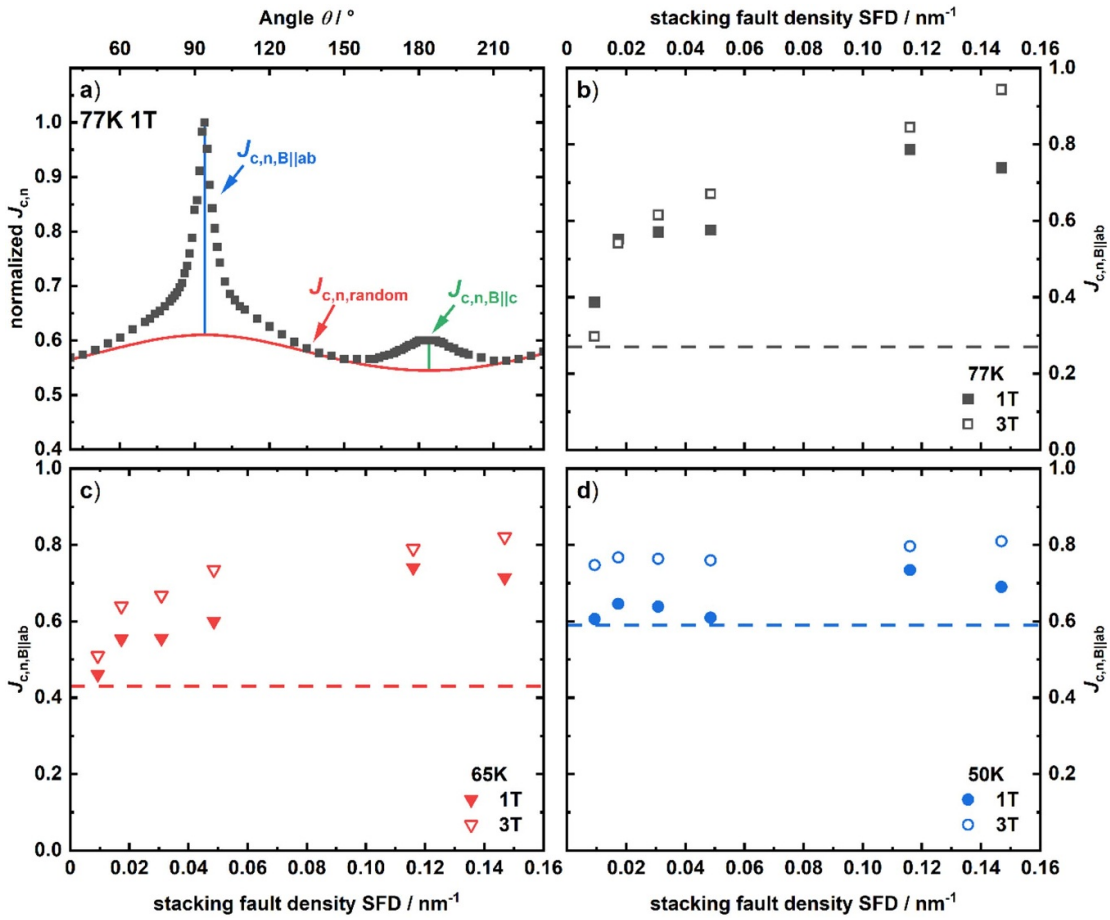

Figure 8. Analysis of contributions to $J_c(\theta)$ by different types of pinning centers. (a) The random pinning contribution, $J_{c,n,random}(\theta)$, was fitted using equation (9) (red line). The peak heights of $J_c(\theta)$ at $\theta = 90°$ and 180° is interpreted as pinning correlated along the *ab*-plane (blue line) and the *c*-axis (green line), respectively. Influence of SFD on $J_c(\theta)$ due to pinning along the *ab*-plane, $J_{c,n,B||ab}$ at (b) 77 K, (c) 65 K and (d) 50 K each at 1 and 3 T. can be further divided into intrinsic (dashed line) and *ab*-plane correlated pinning contributions. The intrinsic pinning proportion of $J_{c,n,B||ab}$ (dashed line) increases while the influence of stacking faults decreases (rise of data points above dashed line) with decreasing temperature. Stacking faults are most effective as *ab*-plane correlated pinning centers at temperatures above 65 K.

$J_{c,n,random}$ shown in figure 8(a)) is an approximation based on the scaling approach of e.g. Aytug *et al* [49] and Civale *et al* [50], which assume that the anisotropy of $J_{c,random}$ follows the anisotropy of B_{irr} scaled by the exponent α, equation (9), which is usually around 0.5. This is valid in the field range of $J_c(\theta)$ power law behavior. γ_{eff} denotes the effective electronic mass anisotropy, which usually assumes values of 5–7 for REBCO but can change drastically due to defects. No qualitative differences are observed for slight changes to α and γ. Therefore, dissecting the normalized $J_{c,n}(\theta)$ curves into the contributions $J_{c,n,random}$, $J_{c,n,B||ab}$ and allows for extracting the influence of the stacking faults.

$$J_{c,random}(\theta) = J_{c,0}[\varepsilon(\theta)]^{-\alpha} = J_{c,0}\left[\cos^2\theta + \gamma_{eff}^{-2}\sin^2\theta\right]^{-\alpha}. \quad (9)$$

The sample with the lowest SFD in figure 7 (grey curve) shows a typical behavior of CSD-REBCO thin films. At 77 K and 1 T, its $J_{c,n,random}(\theta)$ is 0.55 with additional peaks at $B||ab$ and $B||c$ due to correlated pinning. Increasing the magnetic field changes the pinning landscape, which is expressed in an increased anisotropy and lower $J_{c,n,random}(\theta)$. A similar feature is seen when comparing figures 7(c)) and (d)). Lowering the temperature influences which pinning centers are active. Increasing the magnetic field to 3 T leads to a suppression of the $B||c$ peak for the thin films with the lowest SFD. However, more remarkable is the clear sharpening of the $B||ab$ peak. Stacking faults are *ab*-planar defects and lend themselves perfectly as pinning centers at $B||ab$.

The data points in figures 8(b)–(d)) represent the $J_{c,n,B||ab}$ contribution as a function of SFD. At 77 K, $J_{c,n,B||ab}$ increases sharply from 0.3 to 0.6 for SFD = 0–0.06 nm^{-1}, while staying relatively constant at 0.8 for SFD > 0.06 nm^{-1}. The same trend, although less pronounced, is visible at 65 K, figure 8(c)). At 50 K, figure 8(d)), $J_{c,n,B||ab}$ increases only slightly over the whole range of investigated SFD. One possible explanation for the diminishing returns with respect to the increase of $J_{c,n,B||ab}$ is that the pinning

landscape is sufficiently saturated at a SFD of 0.06 nm^{-1} at the investigated magnetic fields. This illustrates that Sm124 stacking faults do not improve the *ab*-correlated pinning indefinitely.

The influence of Sm124 stacking faults on $J_{c,n,B||ab}$ can be further isolated by dividing $J_{c,n,B||ab}$ into a contribution from other sources, e.g. intrinsic pinning, surface pinning and *ab*-extended secondary phases such as Sm_2O_3, and a contribution due to ab-correlated pinning defects such as stacking faults. We use the sample with the lowest SFD as an estimate for the $J_c(\theta)$ contributions due to these other sources (dashed lines figures 8(b)–(d))) and assume that this contribution stays constant for a given T and B. Then, the rise of $J_{c,n,B||ab}$ above the dashed lines in figure 8 can be attributed to the influence of stacking faults.

The level of the intrinsic pinning contribution increases from ~ 0.3 at 77 K to 0.6 at 50 K, which is to be expected, as intrinsic pinning dominates at low temperatures. As already stated, an increasing SFD leads to a rise of $J_{c,n,B||ab}$ at 77 and 65 K, while it remains relatively constant at 50 K. The introduction of Sm124 stacking faults improves the pinning at B||*ab* for $T \geqslant 65$ K.

Lastly, Sm124 stacking fault also seem to influence pinning defects correlated along the *c*-axis. vanishes at SFD $= 0.11$ nm^{-1}, figure 7, which is explained by the fact that the additional CuO layers interrupt *c*-axis-correlated pinning defects [51] such as twin boundaries and hence suppress $J_{c,n,B||c}$.

All these findings are consistent with the literature on pinning [52–54]. The Sm124 phase has a T_c of about 80 K, which leads to δT_c pinning at elevated temperatures [53]. This effect becomes negligible once $T \ll 80$ K, which partially explains the reduced pinning effectiveness of Sm124 stacking faults. The more important effect comes from the intercalated CuO layers in Sm124 stacking faults. The CuO layers separate the superconducting CuO_2 layers further, which leads to a higher energy barrier for the movement of Josephson vortices [52]. In Sm123, these energy barriers can be overcome by thermal fluctuations of the vortex lattice. Thus, Sm124 stacking faults increase the pinning potential of vortices at $T \geqslant 65$ K. The effect of stacking faults decreases with T simply because the thermal fluctuations at low temperatures are not sufficient to overcome the energy barrier for vortex movement in native Sm123 or defect-ridden SmBCO.

5. Discussion

Theory, simulations, and experimental results as well as the validation by transport measurements and TEM give strong evidence that the presented method can accurately determine the density of extended Sm124 stacking faults in Sm123 thin films. By quantifying the microstructure via XRD and by comparing it to literature on stacking faults [34, 48, 55] and pinning [56], a clear understanding of the superconducting behavior of the presented samples is gained.

Even though the presented XRD method produces very consistent results, some experimental findings do not conform to theory and should be discussed. The (003), (009) and (0010) reflections are prone to deviate from the theory, especially in the broadening analysis. The (003) reflection often does not broaden as much as the theory predicts while the (009) and (0010) reflections sometimes broaden significantly more than expected, figure 3. Thus, all available (00 l) reflections should be measured to ensure that the impact of outliers on the peak shift and broadening analysis is mitigated. For satisfactory fits, at least one whole wavelength of the oscillating peak shift and broadening should be recorded, which is at least six (00 l) reflections for RE124 stacking faults.

Comparing the stacking fault frequencies determined by peak shift and broadening, figure 9, reveals a surprising trend. According to theory, both should concur for a single sample, but the stacking fault frequencies determined by broadening f_{FWHM} are consistently smaller than those determined by peak shift f_{PS}. In fact, f_{FWHM} seems to be proportional to f_{PS}^2, dotted line in figure 9. This trend is consistent for both solution types, which indicates that the observed differences are inherent to the samples themselves. It is unclear why both quantities behave in this fashion.

Tarascon *et al* [14] faced similar issues while investigating stacking faults in BSCCO thin films. The observed reflections did not broaden according to the theory presented in [14]. In the case of the results presented in this study, it is possible that the mismatch between f_{PS} and f_{FWHM} originates from using only the first order approximation of equation (33) (appendix). Alternatively, Δ_{PS} may also be more sensitive to extended stacking faults while Δ_{FWHM} is more sensitive to so-called short stacking faults, which are frequently observed in TEM studies [33, 45, 48, 57]. The hypothesis is that the strain field around a Sm124 stacking fault is strongest at the edges, where the partial dislocations of the intercalated CuO layer are located. Hence, the aspect ratio of a stacking fault determines whether the disruption of the periodicity of the lattice (Δ_{PS}) or the localized variations of the lattice plane spacings (Δ_{FWHM}) dominates.

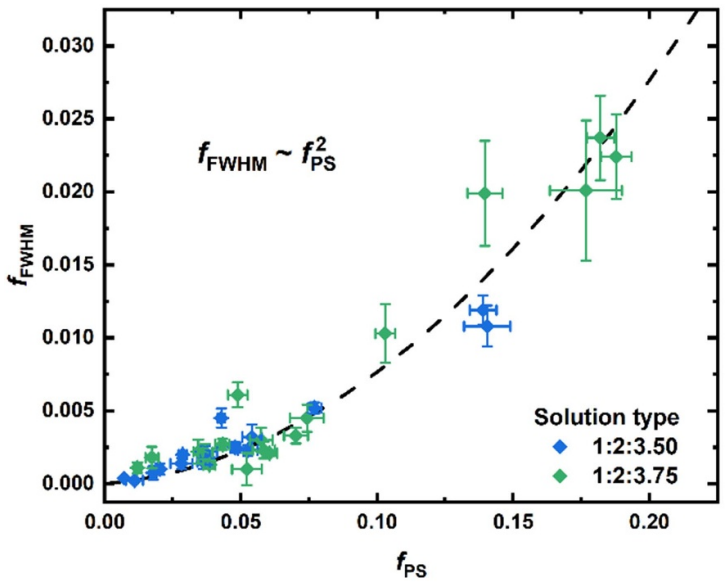

Figure 9. Comparison of the stacking fault frequencies determined by peak shift, f_{PS}, and by broadening, f_{FWHM}, for both solution types. The uncertainty of the fit (two standard deviations) is given with the error bars. The seemingly quadratic proportionality of f_{FWHM} to f_{PS} is shown by the dotted line. The trend is consistent over both solution types.

Table 3. Comparison of SFDs determined by the peak shift Δ_{PS} and broadening Δ_{FWHM} analysis with the SFD determined from TEM micrographs. Four cross-sectional micrographs per sample were investigated to increase the statistical robustness of the SFD_{TEM} values. The estimated errors of the last digits are given in brackets.

	Stacking fault density SFD/nm^{-1}		
Sample	Δ_{PS}	Δ_{FWHM}	TEM
1	0.0512(2)	0.0018(2)	0.000
2	0.1171(7)	0.0092(7)	0.078(20)
3	0.1509(4)	0.0202(4)	0.180(68)

Irrespective of this, figure 9 shows clearly that both quantities are correlated and can be brought into alignment with each other. Knowing that, the simple addition of broadening terms in equation (7) must be regarded as failed. Figure 4(b)) clearly shows that equation (7) correctly describes the oscillating behavior of the integral width with regards to Sm124 stacking faults but the magnitude simply does not add up to the expected value. More theoretical work in understanding the underlying mathematics and more advanced methods of averaging peak widths are needed to solve this issue.

A SFD can be calculated from either stacking fault frequency. Therefore, in order to infer which SFD determined by XRD is more accurate to the actual microstructure, SFDs are determined from TEM micrographs too. The SFD in TEM is calculated by measuring the line density of stacking faults across the film thickness. Thus, SFD_{TEM} represents the mean distance between stacking faults along the *c*-axis, which is synonymous with SFD_{XRD} obtained from $\theta/2\theta$ scans. The TEM imaging difficulties described above resulted in images of sufficient quality to gain the SFD for only three samples, table 3. To increase the statistical robustness, four cross-section micrographs of each sample were investigated to derive the values. Admittedly, the values gathered from three samples or twelve micrographs are statistically still too few to definitively confirm f_{PS} or f_{FWHM}, but it gives crucial evidence about the magnitude of SFD_{TEM}.

It is found that the SFD determined from Δ_{PS} is backed up by the local analysis of TEM micrographs for two samples. Extended stacking faults were absent for sample 1. For this sample, SFD_{FWHM} is the better representation but it must be noted that this is the sample with the lowest SFD of all investigated samples. So, values close to zero are expected. For the other two samples, SFD_{FWHM} and SFD_{TEM} differ by an order of magnitude while SFD_{PS} and SFD_{TEM} concur relatively well. Hence, the presented method can be cautiously regarded as validated and the *SFD* values derived from the peak shift seem reasonable. However, if XRD and TEM data are available, we encourage the reader to apply the presented method to determine the SFDs themselves and check the validity. This way new insights into the sensitivity of this method may be gained.

The results of this study are gathered from CSD-grown SmBCO thin films. However, the theory behind the quantification method is not dependent on SmBCO, or the thin film preparation. The equations presented above can be used for other REBCO systems. We decided to use SmBCO, because a previous study [33] has shown a tendency of CSD-grown SmBCO thin films to form Sm124 stacking faults. Furthermore, this method should also be applicable beyond thin films. The analysis is sensitive along the stacking direction of the investigated crystal structure. Assuming correctly oriented crystallites in a bulk sample or single crystal would lead to the same type of analysis as presented here on thin films. It should be kept in mind that the TEM results presented here were heavily influenced by FIB-lamella bending and stress relaxation, which most likely influences the TEM-derived SFD values. Thus, differences between the presented thin film samples and fully independent bulk samples are expected. Therefore, we encourage anyone to use the presented method on bulk samples and report on it.

Lastly, CSD was the preferred deposition method, because it enabled a simple way to change the stoichiometry of the resulting REBCO thin films. It is entirely possible that similar results can be gathered from thin film samples prepared by sputtering, PLD, or MOCVD. In terms of testing other deposition methods, the hardest challenge is to find a reliable way to produce RE124 stacking faults, rather than the microstructural investigation itself.

We would like to conclude this analysis by emphasizing a couple of points that are important to accurately apply the presented method. First and foremost, it is very important to include as many (00 l) reflections as possible, because the frequency of outliers increases with SFD. Especially the reflections with a low structure factor ((002), (004) and (008)) or reflections that are most affected by broadening ((003) and (009)) are prone to being outliers. For this reason, standard $\theta/2\theta$ measurements should be extended to 120° and slowed down as much as necessary to ensure high signal-to-noise ratios even at high diffraction angles.

A high signal-to-noise ratio is key to detecting and fitting the emerging shoulder peaks at medium to high SFD. During fitting, it is very helpful to stick to symmetric peak shape functions, because inconsistent fits due to peak shift or shoulder peaks become instantly apparent. A shoulder peak fit is necessary whenever a single peak is insufficient to accurately describe the shape of a reflection. It should be noted here that shoulder peaks are not always an indicator for stacking faults. Possible sources of shoulder peaks in REBCO samples are e.g. layers of different oxygen content, *a*-axis grains and secondary phases with unfortunately spaced reflections. The decisive factor is the asymmetry with which such shoulder peaks occur. Differing oxygen contents would always produce shoulder peaks at the same side of a main peak, while stacking fault shoulder peaks occur on either side of a main peak depending on the Miller index.

While the presented method can be used to gain an understanding of the SFD, there are still limitations to the underlying model. The presented theory assumes that the stacking faults are virtually infinite in the *ab*-plane. Our samples are indeed dominated by extended stacking faults, with rare cases of short stacking faults, figure 6. Other TEM studies [33, 45, 48, 57] frequently report short stacking faults with a length of 10–20 nm within the *ab*-plane. It is unclear how these short stacking faults come to be and if and how they influence the diffracted intensity and superconducting properties.

Lastly, equations (5) and (7) represent the simplest case with only a single stacking fault type embedded in the matrix. Multiple kinds of stacking faults can be present and would need higher-order equations to account for the complex interactions between the stacking fault types themselves. Solving the higher-order approximations of equation (31) could help in this regard. We are pleased to share the knowledge we have gained so far in order to develop the work of Hendricks and Teller [29] as well as Suzuki and Suzuki [30] to their full potential.

6. Conclusion

A novel method of quantifying stacking faults is presented. Stacking faults disrupt the periodicity of the lattice along the stacking direction, which leads to phase shifts of the scattered radiation. Those phase shifts translate to peak shifts and peak broadening. We modified the equations developed by Suzuki and Suzuki [30] to fit the problem of *RE*124 stacking faults in *RE*123 (REBCO) thin films. To experimentally confirm this theory, Sm123 thin films with Sm124 stacking faults were produced via Cu excess and high-temperature oxygenation. The SFD was determined using relatively simple XRD scans. TEM identified SFs and precipitates. It was concluded that the SFD determined by peak shift describes the microstructure of the thin films reasonably well.

Being able to quantify stacking faults, makes it possible to analyze the superconducting properties of REBCO based on defect quantities rather than process parameters. This is illustrated by a short analysis

of the influence of stacking faults on the $J_c(\theta)$ anisotropy. Stacking faults are most effective at increasing the *ab*-correlated pinning for temperatures above 65 K. No further significant increase of this type of pinning is observed for stacking fault densities of 0.1 nm^{-1} and above. In the future, we will intensify our efforts to investigate the origin of stacking fault formation upon oxygenation as well as the conditions necessary to produce or avoid RE124 stacking faults.

Acknowledgments

We want to thank Professor M. Suzuki and Dr I. Suzuki for a fruitful correspondence and encouraging us to move forward with this research.

Furthermore, the authors thank Dr E. Mueller for the FIB sample preparation.

Data availability statement

The files needed to recreate the simulations will be shared upon request. The rest of the data cannot be made publicly available upon publication because they are not available in a format that is sufficiently accessible or reusable by other researchers. Much like the simulation files, the data that support the findings of this study are available upon reasonable request from the authors.

Appendix . Scattered intensity of layered crystals

Hendricks and teller

The ground-breaking work on the problem of x-ray scattering on layered crystals with different structure factors and phase shifts was done by Hendricks and Teller in the early 1940s [29]. They formulated an impressive approach to calculate the average scattered intensity. Only the most important equations from Hendricks and Teller will be shown here in order to make it clear how the equations used above are derived. To gain a deeper understanding, the reader is encouraged to follow the well-presented steps in [29].

The x-ray scattering amplitude $|V|$ and phase $\varphi = \exp(iqd_k)$ of the k^{th} layer of a given crystal represented in a vector form are:

$$\overrightarrow{V_k} = |V_k|\ \varphi_k = |V_k| \exp(iqd_k), \tag{10}$$

where q is the scattering vector, and d_k the stacking distance of the k^{th} layer along a stacking direction. It should be noted here that the phase φ may be determined by d_k but also by other factors such as translation of layers along the scattering plane or polarization. These factors are not significant for the problem of stacking faults in REBCO. Thus, we describe φ simply by $\exp(iqd_k)$.

The observable intensity is the absolute square of all layer combinations (k and l) over all n layers:

$$I = \frac{1}{n} \sum_{k=1}^{n} \sum_{l=1}^{n} \vec{V}_k \vec{V}_l^*. \tag{11}$$

If the given crystal is large enough so that n approaches infinity, the double summation can be redefined into a single summation. To do this, the sum of a base vector $\vec{V}_0$ with every other vector of the lattice $\vec{V}_k^*$ may be considered:

$$I = \sum_{k=-\infty}^{+\infty} \frac{1}{2} \left(\vec{V}_0 \vec{V}_k^* + \vec{V}_0^* \vec{V}_k \right) = \sum_{k=-\infty}^{+\infty} |V_k||V_0| \cos(q(d_k - d_0)). \tag{12}$$

The average intensity I_{ave} can be found if equation (12) is averaged over all layer combinations, which depends on the assumed boundary conditions. The first two sections of [29] show the mathematical basics of averaging with different boundary conditions, section 3 holds the first phenomenological insight.

Consider a finite crystal of n layers consisting of r different layer types and therefore r different d_k. Thereby, the scattered intensity of such a crystal may be found by evaluating all combinations of scattering vectors of each layer permutating their type (s and t) and position (k and l). It should be clarified

that s denotes the type of the first and t the type of the second layer of a permutation in order to capture all possible layer type combinations. The scattering vector of the layer at the kth (type s) and lth (type t) position is herein described by $\vec{V}_s$ and $\vec{V}_t^*$ respectively, while the phase shift is represented by $\exp(iq(k-l)\vartheta)$, equation (13). Each layer type has an independent probability of occurring, $\sum_s^r f_s = 1$, resulting in equation (14). Averaging over s and t must be performed to get I_{ave}:

$$I = \frac{1}{n}\sum_{k=1}^{n}\sum_{l=1}^{n}\vec{V}_s\,\vec{V}_t^{\,*}\exp(i(k-l)\vartheta) \tag{13}$$

$$I_{\text{ave}} = \frac{1}{n}\sum_{k,l=1}^{n}\sum_{s,t=1}^{r} f_s\,\vec{V}_s\,f_t\,\vec{V}_t^*\exp(i(k-l)\vartheta) + \frac{1}{n}\sum_{k=1}^{n}\sum_{s=1}^{r} f_s\,|V_s|^2. \tag{14}$$

To average over s and t, it is useful to transform the scattering vectors $\vec{V}_s$ into an average scattering vector and to define a term, $\vec{W}_s$, that captures the differences of each scattering vector $\vec{V}_s$ and the average $\vec{U}$ (These differences then add up to zero):

$$\vec{V}_s = \vec{U} + \vec{W}_s \text{ with } \vec{U} = \sum_{s=1}^{r} f_s\,\vec{V}_s \text{ and } \sum_{s=1}^{r} f_s\,\vec{W}_s = 0. \tag{15}$$

This way, equation (14) can be split and simplified to:

$$I_{\text{ave}} = \frac{1}{n}\sum_{k=1}^{n}\sum_{l=1}^{n}|U|^2\exp(i(k-l)\vartheta) + \sum_{s=1}^{r} f_s\left|\vec{W}_s\right|^2. \tag{16}$$

Thus, Hendricks and Teller show that the average scattered intensity of a layered crystal behaves according to a regular crystal with an averaged structure factor $|U|^2$ and additional, independently scattering layers with the structure factors $\left|\vec{W}_s\right|^2$, which represent the difference between the real structure factors and the average structure factor $\vec{U}$.

Section 4 introduces the so-called matrix method [58], which was later used by Suzuki and Suzuki [30] to develop their peak shape analysis for the problem of intercalated graphite layers.

In this section, correlated stacking with dependent probabilities $P_k^{(st)}$ is introduced. Note, f will be used to describe independent probabilities of any layer type occurring, while P will be used to denote dependent probabilities. Thereby, $P_k^{(st)}$ represent the probability of the kth neighboring layer being type t if the reference layer is type s. One could assume that the scattered intensity of the k^{th} neighbors only depends on the layers themselves, but this is not true. In fact, the scattered radiation of all layers that lie between k^{th} neighbors also contribute to the phase shift. Thereby, $\varphi_k^{(st)}$ describes the phase shift between a layer of type s and its neighbor of type$t$. All possible layer type combinations need to be considered to calculate $\varphi_k^{(st)}$. This can be done, mathematically speaking, by matrix multiplication. Thus, the matrices F (diagonal matrix with $f_{ss} = f_s$), V, and Q_k are introduced to facilitate the averaging of the structure factors and the phase shifts respectively:

$$(VF)_{st} = f_s\,\vec{V}_s\,\vec{V}_t^* \tag{17}$$

$$Q_k^{(st)} = (P\Phi)_k^{(st)} = P_k^{(st)}\exp\left(i\varphi_k^{(st)}\right). \tag{18}$$

Using these formulations, the average intensity is found by averaging the scattering over all possible layer combinations (compare equation (12)):

$$I = \sum_{k=-\infty}^{+\infty}\sum_{s,t=1}^{r}(FP)_k^{(st)}\,\frac{1}{2}\left(\vec{V}_0^{(s)}\vec{V}_k^{*(t)} + \vec{V}_0^{*(s)}\vec{V}_k^{(t)}\right). \tag{19}$$

Here $\vec{V}_0^{(s)}$ denotes the scattering vector of the zero th layer of type s. $\vec{V}_k^{(t)}$ is the scattering vector of the kth layer of type t. The introduced matrices emerge if we assume that $\vec{V}_0^{(s)}$ becomes $\vec{V}_s$ while $\vec{V}_k^{*(t)}$ is equal to the product of $\vec{V}_t^*$ with a factor $\exp\left(i\varphi_k^{(st)}\right)$. This transformation shifts the focus away from

averaging over k layers towards the consideration of the general scattering of type s and type t layers with the additional influence of interference due to neighboring layers. We can simplify the sum of equation (19) by rearranging and explicitly writing out the term for $k = 0$ and splitting the sum of complex conjugates into two sums of complex conjugates:

$$I_{\text{ave}} = \sum_{s=1}^{r} f_s \left| V_0^{(s)} \right|^2 + \sum_{k=1}^{\infty} \sum_{s,t=1}^{r} f_s \, \vec{V}_s \, \vec{V}_t^{*} P_k^{(st)} \exp\left(i\varphi_k^{(st)} \right) + \sum_{k=1}^{\infty} \sum_{s,t=1}^{r} f_s \, \vec{V}_s^{*} \, \vec{V}_t \, P_k^{(st)} \exp\left(-i\varphi_k^{(st)} \right) \tag{20}$$

$$I_{\text{ave}} = \sum_{s=1}^{r} f_s \, |V_s|^2 + \sum_{k=1}^{\infty} \sum_{s,t=1}^{r} (VF)_{st} Q_k^{(st)} + \sum_{k=1}^{\infty} \sum_{s,t=1}^{r} (VF)_{st}^{*} Q_k^{*(st)}. \tag{21}$$

Hendricks and Teller show that the matrix elements $Q_k^{(st)}$ are connected to $Q_{k+1}^{(st)}$ via $Q_{k+1}^{(st)} = \sum_q^r Q_k^{(sq)} Q_1^{(qt)}$. This means that the matrix Q_k can be described as $Q_k = (Q_1)^k$ (see [29] for details). By multiplying Q_1 with itself k times, all layer type combinations of k^{th} neighbors and their in-between layers are considered and equation (21) becomes:

$$\begin{aligned} I_{\text{ave}} &= \sum_{s=1}^{r} f_s \, |V_s|^2 + \sum_{k=1}^{\infty} \sum_{s,t=1}^{r} (VF)_{st} Q_1^k + \sum_{k=1}^{\infty} \sum_{s,t=1}^{r} (VF)_{st}^{*} (Q_1^{*})^k \\ &= \sum_{s=1}^{r} f_s \, |V_s|^2 + \sum_{k=1}^{\infty} \text{spur}\left((VF) \, Q_1^k \right) + \sum_{k=1}^{\infty} \text{spur}\left((V^{*}F) \, (Q_1^{*})^k \right). \end{aligned} \tag{22}$$

Looking at the elements of $(FV)_{st} Q_1^k$ shows that only the main diagonal elements represent valid layer combinations. Therefore, the sum reduces to the trace, or *spur*, of the matrix product, $\text{spur}\left(FVQ_1^k\right)$. The final transformation can be done by diagonalizing Q_1 with the matrices O and O^{-1} and flipping the summation over k and the *spur*. The diagonal matrix D contains the eigenvalues of Q_1. Through that, Neumann series (geometric series for matrices) are formed:

$$O^{-1} Q_1 O = D = \text{diag}\left(\lambda_1, \lambda_2, \ldots, \lambda_r\right) \; \textit{and} \; O^{-1} FVO = R \tag{23}$$

$$\begin{aligned} I_{\text{ave}} &= \sum_{s=1}^{r} f_s |V_s|^2 + \text{spur}\left(\sum_{k=1}^{\infty} O^{-1} VFOD^k \right) + \text{spur}\left(\sum_{k=1}^{\infty} O^{-1} (VF)^{*} O (D^{*})^k \right) \\ &= \sum_{s=1}^{r} f_s |V_s|^2 + \text{spur}\left(\sum_{k=1}^{\infty} RD^k \right) + \text{spur}\left(\sum_{k=1}^{\infty} R^{*} (D^{*})^k \right) \end{aligned} \tag{24}$$

$$I_{\text{ave}} = \sum_{s=1}^{r} f_s |V_s|^2 + \sum_{s=1}^{r} \frac{R_{ss} D_s}{1 - D_s} + \sum_{s=1}^{r} \frac{R_{ss}^{*} D_s^{*}}{1 - D_s^{*}}. \tag{25}$$

The average intensity can therefore be described by a regular crystal with an average structure factor (first term) plus interference terms (2 nd and 3rd terms). From equation (25) it becomes clear that sharp intensity maxima emerge by interference when D_s approaches 1 given that $R_{ss} D_s$ does not vanish.

Suzuki and Suzuki

Suzuki and Suzuki [30] applied this approach to graphite intercalation compounds (GICs) to approximate the influence of randomly intercalated graphite layers. To do this, r intercalation layers with corresponding phase shifts and stacking distances d_r need to be considered, $\varphi_{st} = \varphi_s = \exp(iqd_s)$. The stacking probabilities are defined similar to Hendricks and Teller [29]:

$$\sum_s f_s = 1 \qquad \sum_t P_{st} = 1 \qquad \sum_s f_s P_{st} = f_t \; . \tag{26}$$

f_s denotes the independent probability of any layer being of type s. P_{st} is the dependent probability of a layer being type t if the previous layer was of type s. Using the matrices introduced in equations (17) and (18), we arrive at equation (22) once more. Note that if $P_{st} = f_t$, no correlated stacking occurs, and a random distribution of layer types is assumed and Q of equation (22) becomes $Q_{st} = (P\Phi)_{\text{st}} = P_{\text{st}} \varphi_{st} =$

$f_t\varphi_s = f_t\exp(iqd_s)$. The assumption of random stacking ensures that Q has only 1 non-zero eigenvalue, which extremely shortens the diagonalization of Q and simplifies the matrix product $O^{-1}VFO$ by reducing the 2nd and 3rd term of equation (25) to a single summand each:

$$O^{-1}QO = D = \mathrm{diag}(\lambda, 0, \ldots 0) \text{ with } \lambda = \sum_r f_r\,\varphi_r. \tag{27}$$

$$\begin{aligned} I(q) &= \sum_{s=1}^{r} f_s|V_s|^2 + \frac{\sum_{s,t}^{r} f_s V_s V_t^* f_t\varphi_s}{1-\sum_r f_r\varphi_r} + \frac{\sum_{s,t}^{r} f_s V_s^* V_t f_t\varphi_s^*}{1-\sum_r f_r\varphi_r^*} \\ &= \sum_{s=1}^{r} f_s|V_s|^2 + 2\mathrm{Re}\left(\frac{\sum_{s,t}^{r} f_s V_s V_t^* f_t\varphi_s}{1-\sum_r f_r\varphi_r}\right) \text{with } z+\bar{z} = 2\mathrm{Re}(z). \end{aligned} \tag{28}$$

$$I(q) = \sum_{s=1}^{r} f_s|V_s|^2 + 2\mathrm{Re}\left(\frac{\chi(q)}{1-\sum_r f_r\varphi_r}\right) \text{with } \chi(q) = \sum_{s,t}^{r} f_s V_s V_t^* f_t\varphi_s. \tag{29}$$

equation (29) is the same as equations (14) and (15) in [30]. The first term describes the regular scattering intensity of the layered crystal with an averaged structure factor. The second term deals with additional intensity due to interference. Additional intensity maxima emerge when $\sum_r f_r\,\varphi_r \approx 1$ with an amplitude of $\chi(q)$.

Evolving equation (29) further by expanding the second term with its complex conjugate yields:

$$\begin{aligned} \mathrm{Re}\left(\frac{\chi(q)}{1-\sum_r f_r\varphi_r}\right) &= \mathrm{Re}\left(\frac{\chi(q)}{1-\sum_r f_r\varphi_r} * \frac{1-\sum_r f_r\varphi_r^*}{1-\sum_r f_r\varphi_r^*}\right) \\ &= \frac{\mathrm{Re}(\chi(q))\left(1-\sum_r f_r\cos(qd_r)\right) - \mathrm{Im}(\chi(q))\left(\sum_r f_r\sin(qd_r)\right)}{\left(1-\sum_r f_r\cos(qd_r)\right)^2 + \left(\sum_r f_r\sin(qd_r)\right)^2}. \end{aligned} \tag{30}$$

$$I(q) = \sum_{s=1}^{r} f_s|V_s|^2 + 2\frac{\mathrm{Re}(\chi(q))\left(1-\sum_r f_r\cos(qd_r)\right) - \mathrm{Im}(\chi(q))\left(\sum_r f_r\sin(qd_r)\right)}{\left(1-\sum_r f_r\cos(qd_r)\right)^2 + \left(\sum_r f_r\sin(qd_r)\right)^2}. \tag{31}$$

While this seems cumbersome at first, Suzuki and Suzuki realized the second term of equation (31) resembles a Lorentzian peak shape if the frame of reference is changed from a general point of view, q-space, to the influence of intercalated layers around reflections of a dominant phase ($f_u \approx 1$), which occur at $q_L^{(u)} = \frac{2\pi l}{d_u}$.

Comparing equation (31) to the general form of a symmetric Lorentzian peak shape,

$$L(q) = \frac{Amplitude}{Width^2 + (q - q_{\mathrm{center}})^2},. \tag{32}$$

it becomes clear that a centering must be introduced while the second part of the denominator must describe the broadening., as a symmetric function, can be used to describe the symmetric broadening due to intercalated layers. The centering is performed by introducing $q - q_L^{(u)}$ into the second term of the denominator. Suzuki and Suzuki proposed:

$$I(q) = \sum_{s=1}^{r} f_s|V_s|^2 + \frac{2}{f_u d_u}\frac{\mathrm{Re}(\chi(q))(\Gamma(q)) - \mathrm{Im}(\chi(q))\left(q - q_L^{(u)} - \Sigma(q)\right)}{(\Gamma(q))^2 + \left(q - q_L^{(u)} - \Sigma(q)\right)^2}. \tag{33}$$

$$\Sigma(q) = -\frac{1}{f_u\,d_u}\sum_r f_r\sin(qd_r) + \left(q - q_L^{(u)}\right). \tag{34}$$

$$\Gamma(q) = \frac{1}{f_u\,d_u}\left(1-\sum_r f_r\cos(qd_r)\right) = \frac{1}{f_u\,d_u}\sum_r f_r(1-\cos(qd_r)). \tag{35}$$

It becomes apparent that the intercalated layers shift the peaks of the dominant phase by $\Sigma(q)$ and broaden its peaks by $\Gamma(q)$. The scaling factor $1/(f_u\, d_u)$ is introduced due to the changed frame of reference. It provides the correct unit for each part of the peak shape function.

If the Lorentzian is now evaluated around $q_L^{(u)}$, the second term of $\Sigma(q)$ vanishes, and peak shift (Δ_{PS}) as well as change in FWHM (Δ_{FWHM}) can be described as:

$$\Delta_{PS} = \Sigma(q_L^u) \qquad \Delta_{FWHM} = 2\Gamma(q_L^u)\ . \tag{36}$$

Just for clarity: If only the dominant phase exists, then $q_L^u d_r = \frac{2\pi l}{d_u} d_u = 2\pi l$ and Δ_{PS} and Δ_{FWHM} vanish due to $\sin(2\pi l) = 0$ and $1 - \cos(2\pi l) = 0$. In case of multiple layers, only the difference in stacking distance Δd is relevant for the calculation of Δ_{PS} and Δ_{FWHM} by:

$$d_r = d_u + \Delta d \rightarrow \begin{matrix}\sin\\ \cos\end{matrix}\left(\frac{2\pi l}{d_u}(d_u + \Delta d)\right) = \begin{matrix}\sin\\ \cos\end{matrix}\left(\frac{2\pi l}{d_u}\Delta d\right). \tag{37}$$

Furthermore, Suzuki and Suzuki show a higher order approximation for and Δ_{FWHM}, while equations (34) and (35) only describe the 1st order approximation. Unfortunately, the paper does not show how the authors derived their higher-order approximation, which might be useful for more complex problems in the future. However, for the purposes of this paper, the 1st order approximation suffices.

ORCID iDs

Kai Walter 0009-0004-5366-6639
Mark Rikel 0000-0002-4537-0772
Martin Peterlechner 0000-0002-4019-8811
Manuela Erbe 0000-0001-9698-1509
Jens Hänisch 0000-0003-2757-236X
Bernhard Holzapfel 0000-0002-8420-4777

References

[1] Jorgensen J, Veal B, Nowicki L, Paulikas A, Crabtree G and Kwok W 1990 *Phys. Rev. B* **41** 1863–77
[2] Veal B W and Paulikas A P 1991 *Physica C* **184** 321–31
[3] Cava R J, Hewat A W, Hewat E A, Batlogg B, Marezio M, Rabe K M, Krajewski J J, Peck W F and Rupp L W 1990 *Physica C* **165** 419–33
[4] Walter K, Erbe M, Welle A, Hänisch J and Holzapfel B 2024 *Supercond. Sci. Technol.* **37** 75002
[5] Dimos D, Chaudhari P and Mannhart J 1990 *Phys. Rev. B* **41** 4038–49
[6] Verbist K, Vasiliev A L and Van tendeloo G 1995 *Appl. Phys. Lett.* **66** 1424–6
[7] Majkic G, Yao Y, Liu J, Liu Y, Khatri N D, Shi T, Chen Y, Galstyan E, Lei C and Selvamanickam V 2013 *IEEE Trans. Appl. Supercond.* **23** 6602605
[8] Majkic G, Jeong J S, Yun H, Robles H F C, Galstyan E, Pratap R, Cheng H, Stokes A, Mkhoyan K A and Selvamanickam V 2021 *Supercond. Sci. Technol.* **34** 115002
[9] Jia C L, Soltner H, Kabius B, Poppe U, Urban K and Schubert J 1991 *Physica C* **182** 163–70
[10] Routbort J L and Rothman S J 1994 *J. Appl. Phys.* **76** 5615–28
[11] Wimbush S C, Li M C, Vickers M E, Jia Q X and MacManus-Driscoll J L 2008 *J. Phys.: Conf. Ser.* **97** 12214
[12] Wimbush S C, Li M, Vickers M E, Maiorov B, Feldmann D M, Jia Q and MacManus-Driscoll J L 2009 *Adv. Funct. Mater.* **19** 835–41
[13] Dric V A 1990 *X-ray Diffraction by Disordered Lamellar Structures: Theory and Applications to Microdivided Silicates and Carbons* (Springer)
[14] Tarascon J M, McKinnon W R, Barboux P, Hwang D M, Bagley B G, Greene L H, Hull G W, LePage Y, Stoffel N and Giroud M 1988 *Phys. Rev. B* **38** 8885–92
[15] Rikel M O and Hellstrom E E 2001 *Physica C* **357–360** 1081–90
[16] Kulakov A B, Maier D, Maljuk A, Bdikin I K and Lin C T 2006 *J. Cryst. Growth* **296** 69–74
[17] Manaila R, Miu L and Zaharescu M 1991 *J. Mater. Sci.* **26** 4136–41
[18] Manaila R, Malis O, Manciu M and Devenyi A 1995 *Phys. Status Solidi* **147** 31–43
[19] Malis O, Manciu M, Manaila R and Devenyi A 1995 *Phys. Status Solidi* **147** 325–33
[20] Specht E D, Goyal A, Li J, Martin P M, Li X and Rupich M W 2006 *Appl. Phys. Lett.* **89** 162510
[21] Wee S H, Specht E D, Cantoni C, Zuev Y L, Maroni V, Wong-ng W, Liu G, Haugan T J and Goyal A 2011 *Phys. Rev. B* **83** 224520
[22] Rikel M O, Amelichev V A, Markelov A V, Degtyarenko P N, Adamenkov A A and Kamenev A A 2024 *IEEE Trans. Appl. Supercond.* **34** 1–5
[23] Ariosa D, Tsaneva V N and Barber Z H 2005 *IEEE Trans. Appl. Supercond.* **15** 2993–6
[24] Rumble J R 2023 *CRC Handbook of Chemistry and Physics* (CRC Press)
[25] Marsh P, Fleming R M, Mandich M L, DeSantolo A M, Kwo J, Hong M and Martinez-Miranda L J 1988 *Nature* **334** 141–3
[26] Yu J, Park K T and Freeman A J 1991 *Physica C* **172** 467–76

[27] Morris D E, Asmar N G, Nickel J H, Sid R L, Wei J and Post J E 1989 *Physica C* **159** 287–94
[28] MacManus-Driscoll J L and Wimbush S C 2021 *Nat. Rev. Mater.* **6** 587–604
[29] Hendricks S and Teller E 1942 *J. Chem. Phys.* **10** 147–67
[30] Suzuki I S and Suzuki M 1991 *J. Phys.: Condens. Matter* **3** 8825–39
[31] Harrington G F and Santiso J 2021 *J. Electroceram.* **47** 141–63
[32] Talantsev E F, Wimbush S C, Strickland N M, Xia J A, D'souza P, Storey J G, Tallon J L, Ingham B, Knibbe R and Long N J 2013 *IEEE Trans. Appl. Supercond.* **23** 7200205
[33] Hänisch J, Iida K, Cayado P, Erbe M, Grünewald L, Hatano T, Okada T, Gerthsen D, Awaji S and Holzapfel B 2022 *Supercond. Sci. Technol.* **35** 84009
[34] Puichaud A-H, Wimbush S C and Knibbe R 2017 *Supercond. Sci. Technol.* **30** 1–9
[35] Chen J, Huang R, Shen J, Qian S, Li M, Fan F, Bai C, Liu Z and Cai C 2021 *Appl. Phys. Express* **14** 55506
[36] Casas-cabanas M, Rodríguez-carvajal J and Palacín M R 2006 *Z. Kristallogr. Suppl.* **2006** 243–8
[37] Treacy M M J, Newsam J M and Deem M W 1991 *Proc. R. Soc. A* **433** 499–520
[38] Erbe M, Hänisch J, Freudenberg T, Kirchner A, Mönch I, Kaskel S, Schultz L and Holzapfel B 2014 *J. Mater. Chem. A* **2** 4932
[39] Walter K, Erbe M, Hänisch J and Holzapfel B 2025 *IEEE Trans. Appl. Supercond.* **35** 1–5
[40] Popov R, Ackermann K, Rijckaert H, Hänisch J, van Driessche I and Holzapfel B 2020 *J. Phys.: Conf. Ser.* **1559** 12038
[41] de la Peña F *et al* 2016 *Hyperspy: HyperSpy 0.8.4* Zenodo
[42] Du H 2015 *Ultramicroscopy* **151** 62–67
[43] Matsumoto O, Utsuki A, Tsukada A, Yamamoto H, Manabe T and Naito M 2008 *Physica C* **468** 1148–51
[44] Matsumoto O, Utsuki A, Tsukada A, Yamamoto H, Manabe T and Naito M 2009 *Physica C* **79** 100508
[45] Holesinger T G *et al* 2008 *Adv. Mater.* **20** 391–407
[46] Soman A A, Wimbush S C, Rupich M W, Notthoff C, Kluth P, Knibbe R, Li M and Strickland N M 2022 *IEEE Trans. Appl. Supercond.* **32** 1–5
[47] Mellekh A, Ben Salem M and Zouaoui M 2019 *IEEE Trans. Appl. Supercond.* **29** 1–6
[48] Zhu Y, Tsai C-F and Wang H 2013 *Supercond. Sci. Technol.* **26** 25009
[49] Aytug T *et al* 2006 *Phys. Rev. B* **74** 184505
[50] Civale L *et al* 2004 *J. Low Temp. Phys.* **135** 87–98
[51] Rouco V, Palau A, Guzman R, Gazquez J, Coll M, Obradors X and Puig T 2014 *Supercond. Sci. Technol.* **27** 1–7
[52] Buckel W and Kleiner R 2013 *Supraleitung: Grundlagen Und Anwendungen (Lehrbuch Physik)* 7th edn (Wiley)
[53] Griessen R, Wen H, van Dalen A J, Dam B, Rector J, Schnack H G, Libbrecht S, Osquiguil E and Bruynseraede Y 1994 *Phys. Rev. Lett.* **72** 1910–3
[54] Huijbregtse J M, Klaassen F C, Szepielow A, Rector J H, Dam B, Griessen R, Kooi B J and de Hosson J T M 2002 *Supercond. Sci. Technol.* **15** 395–404
[55] Guzman R, Gazquez J, Rouco V, Palau A, Magen C, Varela M, Arbiol J, Obradors X and Puig T 2013 *Appl. Phys. Lett.* **102** 81906
[56] Feighan J P F, Kursumovic A and MacManus-Driscoll J L 2017 *Supercond. Sci. Technol.* **30** 123001
[57] Cayado P, Grünewald L, Erbe M, Hänisch J, Gerthsen D and Holzapfel B 2022 *RSC Adv.* **12** 28831–42
[58] Kakinoki J and Komura Y 1952 *J. Phys. Soc. Jpn.* **7** 30–35